Dalton Transactions

Tuning the Mn valence state in new Ca0.66Mn2-xAlxO4 (x≤0.4) oxides: impact on magnetic and redox properties

Journal:	*Dalton Transactions*
Manuscript ID	DT-ART-07-2015-002761.R3
Article Type:	Paper
Date Submitted by the Author:	07-Jan-2016
Complete List of Authors:	DEMOURGUES, Alain; ICMCB-CNRS-University of Bordeaux I, Lesturgez, Stéphanie; ICMCB-CNRS-Univesity of Bordeaux, Goglio, Graziella; ICMCB CNRS, Université de Bordeaux WEILL, François; CNRS, ICMCB N'Guyen, Olivier; ICMCB-CNRS-Univesity of Bordeaux, Toulemonde, Olivier; ICMCB, ; Universté de Bordeaux , Durand, Etienne; ICMCB-Univ Bordeaux, Hernandez, Julien; SOLVAY-Aubervilliers Research Center,

Tuning the Mn valence state in new $Ca_{0.66}Mn_{2-x}Al_xO_4$ (x≤0.4) oxides: impact on magnetic and redox properties.

Stéphanie Lesturgez[1,2], Graziella Goglio[1,2], François Weill[1,2], Olivier N'Guyen[1,2], Olivier Toulemonde[1,2] , Etienne Durand[1,2] , Julien Hernandez[3] and Alain Demourgues*[1,2]

[1]CNRS, ICMCB, UPR 9048, F33600 Pessac, France
[2]Univ. Bordeaux, ICMCB, UPR 9048, F33600 Pessac, France
[3]SOLVAY, Centre de Recherche et Innovation de Paris Aubervilliers, 52 Rue de la Haie Coq, 93306 Aubervilliers Cedex, France

Table of contents (TOC)

Stéphanie Lesturgez, Graziella Goglio, François Weill, Olivier N'Guyen, Olivier Toulemonde, Etienne Durand, Julien Hernandez and Alain Demourgues*

Submitted to Dalton. Trans

Tuning the Mn valence state in new $Ca_{0.66}Mn_{2-x}Al_xO_4$ (x≤0.4) oxides and impact on magnetic and redox properties

The Al^{3+} substitution for Mn^{4+}/Mn^{3+} into the $Ca_{0.66}Mn_2O_4$ 1D tunnel network leads to the stabilization of an orthorhombic unit cell (SG : Pnma) with two various Mn sites attributed mainly to Mn^{4+} and Mn^{3+} respectively. The higher the Al content, the higher the Mn valence state in the same site as Al, the lower the antiferromagnetic interchain interactions at low temperature between two rutile double chains. Redox cycling properties between these Mn^{4+}/Mn^{3+} phases and Mn^{2+} rocksalt solid solution have been demonstrated.

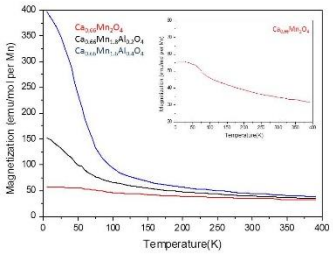

Keywords : Manganese mixed valence, Ca vacancies, Magnetic properties, Tunnel structure, Rocksalt network, Redox properties

Abstract

New $Ca_{0.66}Mn_{2-x}Al_xO_4$ ($x \leq 0.4$) solid solutions crystallizing with the $CaFe_2O_4$-type structure (SG: *Pnma*) were synthesized for the first time by Glycine-Nitrate Process. The structures were determined on the basis of XRD Rietveld analysis and electron diffraction investigation. While the $CaMn_3O_6$ ('$Ca_{0.66}Mn_2O_4$') oxide adopts a monoclinic unit cell, the Al substitution for Mn (x=0.2, 0.4) leads to an orthorhombic cell with only two Mn atomic positions, with various valence states, and 33% of Ca sites empty. The Ca molar concentration decreases down to 0.6 in order to increase the Mn valence leading to a phase mixture, whereas a slight Ca content increase up to 0.7 is compatible with a decrease of Mn valence in the pure phase. The Al^{3+} ions are located in a specific Mn site because of their ionic radii close to that of Mn^{4+} and a more isotropic environment. The unit cell parameters and volume strongly decrease for low Al content and tend to an asymptotic value for x=0.33-0.4, around the limit of solubility. As the Al content increases, the Mn valence state in the same slightly distorted octahedral site increases up to 4+ whereas the other octahedral site is highly elongated and corresponds mainly to Jahn-Teller Mn^{3+}. At x=0.33, these two Mn sites correspond to Mn^{4+} and Mn^{3+} respectively. Moreover, the aluminium content increase induces a weakening of the global antiferromagnetic long range interactions between ferromagnetic chains. The Al substitution leads to the change of the Mn valence distribution as well as the unit cell symmetry of the $CaMn_3O_6$ phase. These 1D tunnel networks stabilizing the Mn^{3+}/Mn^{4+} valence states can be reduced under $Ar/5\%H_2$ between T=300°C and T= 600°C (heating rate = 2°C/min) into pure Mn^{2+} rocksalt solid solution despite the large difference of ionic radii. The re-oxidation leads to the same $CaFe_2O_4$-type structure and several redox cycles can be operated. The relationship between the two double chains of edge-sharing octahedral sites and the rocksalt-type framework is clear and should appear as the driving force of the structural transformation during the reduction/oxidation processes. Finally, the Al substitution allows an increasing of the Mn-O bond covalence and consequently the reduction temperature.

Introduction

Ceria (CeO_2) being well established as an oxygen buffer is widely used as a base oxide in catalysis in which oxidation-reduction process are involved [1,2]. The capability to store oxygen ions and the creation of anionic vacancies in the fluorite-type networks are associated with the valence change of Ce between Ce^{4+} ($4f^0$) and Ce^{3+}($4f^1$) ions [3]. In order to improve the reducing properties, the oxygen storage capacity (OSC) and the thermal stability of Cerium oxide, the $Ce_{1-x}Zr_xO_2$ solid solutions have been widely investigated [4,5]. It was shown that cation site distortions, as well as cationic ordering, play a key role on redox properties. More recently, because of Pr^{4+}'s ($4f^1$) higher fourth ionization potential, which is likely less stable and easier to reduce, the $Pr_{1-x}Zr_xO_{2-y}$ solid solution was studied in order to show the impact of Pr cations on redox properties [6]. As expected, the Pr^{4+} reduction in these oxides occurs for $300°C \leq T \leq 550°C$ whereas the Ce^{4+} reduction takes place mainly at $T \geq 450°C$ [6].

In place of the fluorite network oxides with rare-earth ions as reducible species, the perovskite oxides with Mn^{3+} and Mn^{4+} ions were investigated by redox processes mainly because Mn^{4+} ($3d^3$) can be stabilized at high temperatures under air and exhibits a larger fourth ionization potential than Ce^{4+} and Pr^{4+} respectively. Furthermore the intermediate reduced state, Mn^{3+} ($3d^4$), corresponds to a Jahn-Teller ion stabilized in distorted octahedral and/or pentahedral sites due to the stabilization of oxygen vacancies [7-9]. This distortion is expected to favor the oxygen mobility into the oxide networks [8]. Particularly, topotactic $CaMnO_3$-$CaMnO_2$ reduction-oxidation cycles occur between perovskite-type and rock-salt type networks showing the occurrence of short range ordered domains with peculiar Ca/Mn organization into a NaCl-type matrix [10]. The description of the rocksalt-type structure by stacking Ca/Mn planes along the (111) direction shows a clear relationship with the perovskite-type network [10]. Moreover, the Mn^{4+} reduction under Ar/H_2 atmosphere

in $CaMnO_3$ begins at moderate temperature around T=400°C and reaches Mn^{2+} state in $CaMnO_2$ at T=650°C.

In the alkaline earth series, the choice of Ca^{2+} associated with Mn^{4+}/Mn^{3+} valence states is among the most promising to get the lowest reduction temperatures because of its smaller ionic radius creating less Ca-O ionic bonding (compared to Sr-O or Ba-O). This induces more ionic $Mn^{4+/3+}$-O bonds and leads to the reduction of Mn at lower temperatures [11]. In order to increase the concentration of reducible species, special attention has been paid to the phases with an atomic ratio Mn/Ca >>1. That is why the Ca-Mn-O phase diagram proposed by Horowitz and Longo [12] was investigated, identifying several line compounds in the Mn-rich region with a 1D tunnel structure-type. $CaMn_2O_4$ (SG: Pbnm, one Mn^{3+} crystallographic site) [13-16] and/or $CaMn_3O_6$ (SG: P21/a, two $Mn^{(4-\delta)+}$ and four $Mn^{(3+\delta)+}$ crystallographic sites) compounds are built from double rutile chains forming the 3D framework enclosing Ca^{2+} ions. These ions are located in the 1D channels and have an eight-fold coordination with oxygen ions [17]. Consequently, the connectivity with edge-sharing and corner-sharing MnO_6 octahedra characterizing these 1D tunnel structures differs from that identified in the $CaMnO_3$ perovskite. The relationship with the rocksalt-type network is evident from the double rutile chains. Each octahedron shares four edges with other octahedral with M-M distances (M = transition metal) varying from 2.8 to 3.2 Å [13,17-18].

To improve the redox properties, starting from $CaMn_3O_6$ compounds, there are two ways that can be considered to increase the Mn^{4+} content. One consists in decreasing the Ca concentration [12,19-20] to reach a Ca/Mn atomic ratio equal to 1/4 ($CaMn_4O_8$). Here another tunnel structure is stabilized with two kinds of architecture for the channels : single chains of edge-sharing ($Mn^{4+}O_6$) octahedra and single chains of edge-sharing ($Mn^{3+}O_5$) pyramids with a high tendency of charge ordering of the manganese ions [20]. One other way is substituting lower valence cations for Mn sites such as Fe^{3+} or Al^{3+}. Interestingly, a solid state chemistry investigation of $Ca_{1-y}Mn_{2-x}Fe_xO_4$ ($0 \leq x \leq 1.55$) solid solutions was recently done. It was shown that the oxides adopt the $CaFe_2O_4$-type structure where the number of Ca-vacancies (y) increases with Mn content and tends to y = 1/4 for low Fe concentration [21]. Further, the $CaMn_3O_6$ framework with six $Mn^{4+/3+}$ various atomic positions derives from $CaFe_2O_4$-type structure (SG: *Pnma*) with only two different Fe^{3+}

crystallographic sites [13,17-18]. The $CaMn_3O_6$ tunnel structure contains cationic vacancy ordering located in the 1D-channels with a 1-2-type ordering of one vacancy and two calcium ions giving the chemical formula $Ca_{2/3}Mn_2O_4$ which describes the relationship with $CaFe_2O_4$-type structure.

The approach reported here is dedicated to Al^{3+} substitution in order to understand the dependence on the redox properties of $Mn^{2+/3+/4+}$ on Al content. Therefore, the $Ca_{2/3}Mn_{2-x}Al_xO_4$ solid solution has been investigated by fixing a lower Ca content in order to increase the Mn valence. In this study, we discuss the synthesis and structural characterization by transmission electron microscopy and Rietveld refinement of powder XRD diagrams. The analysis of Mn/Al local environments and the associated magnetic properties allows the variation of Mn valence states to be followed. Finally, the TGA (Thermogravimetric analysis) measurements, under reducing and oxidizing atmosphere, allow the redox properties, which have to be correlated to the chemical composition and the structural features, to be evaluated.

Experimental section

The complex $Ca_{0.66}Mn_{2-x}Al_xO_4$ oxides have been prepared by the self-combustion synthesis method (Glycine Nitrate Process) using glycine [22-24], Ca^{2+} and Mn^{2+} nitrates solutions and $Al(NO_3)_3.9H_2O$ powder. The Ca solution has been accurately titrated by potentiometry using Ca-ion selective electrodes. The Mn content in the solution has been determined by complexometric titration of Mn^{2+} with EDTA (Ethylene Diamine Tetraacetic Acid). Stoichiometric amounts of Ca, Mn and Al nitrates were mixed while stirring. The glycine, in granular form, was added with a glycine/metal molar ratio of 2 in order to ensure optimum cation chelation. The solution was then heated to approximately 100°C to evaporate excess water until a viscous solution was obtained. The gel was introduced into a 4 L stainless steel beaker on a hot plate at 220 °C and self-combustion occurred naturally. The beaker was covered with a stainless-steel openwork lid to contain the as-produced ashes while allowing the departure of gases. The ashes were annealed under air at 850°C for 12 hours.

Powder X-Ray diffraction patterns were collected on a Phillips X'Pert MPD X-ray diffractometer with Bragg-Brentano geometry using Cu $K_{\alpha1}$/ $K_{\alpha2}$ radiation

(10°<2θ<80° range, step of 0.017 ° and counting time of 500s). Three diffractograms (Cu $K_{\alpha 1}$ =1.5406 Å, 10°<2θ<130° range, step of 0.008 ° and counting time of 2000 s) and related structures corresponding to x=0, 0.2 and 0.4 (Al content) compositions have been refined using the Rietveld method and Fullprof package of programs with conventional reliability factors. Unit cell parameters, atomic positions, occupancies and Debye-Waller factors have been refined for each composition. Three different Debye-Waller factors have been determined for Ca, Mn/Al and O atomic positions respectively. The distribution of Al atoms in two various Mn sites were first considered and the partial occupancies then refined. Then, on the basis of Mn/Al-O bond distance analysis, only one atomic position has been taken into account for Al atoms.

Electron diffraction experiments and the reconstruction of reciprocal space were carried out on a JEOL 2100 microscope, equipped with a double tilt specimen stage, operating at 200 kV. The powder was suspended in ethanol and a few drops of this was placed on a carbon- coated copper grid and air-dried before observation.

The magnetization measurements were performed on powder samples with a Quantum Design MPMS-5 (S.Q.U.I.D) magnetometer. Zero-field cooled data were collected with an applied field of 10 kOe and with increasing temperature from 4 K to 400 K. Field dependence on magnetization curves have been recorded with a magnetic field from 0 to 50 kOe at temperatures of 4 K, 150 K and 300 K.

The thermogravimetric analysis (TGA) have been carried out on SETARAM Setsys with evolution under Ar/5% H_2 flux (50 ml/min) and a heating rate of 5°C/min up to 700 °C, then under air (50 ml/min) with a heating rate of 5 °C/min up to 850°C. Other TGA experiments have been performed only under Ar/5% H_2 with a lower heating rate of 2 °C/min in order to compare the reduction steps observed for various compositions.

Results and discussion

Structure analysis by electron diffraction and powder XRD

The comparison between the XRD diagrams of $CaMn_3O_6$ and $Ca_{0.66}Mn_{1.6}Al_{0.4}O_4$ (noted Al04) oxides shows the absence of superstructure diffraction lines at low 2θ angles in the case of the Al-substituted compound (Figure 1 and S1). These superstructure peaks are associated with the monoclinic unit cell

(SG: *P21/a*) for $CaMn_3O_6$ (Figure S2, Table S1). Furthermore, it is noteworthy that several high intensity XRD peaks of Al04 sample exhibit no splitting (see the enlargement around $2\theta=37°$ in Figure 1). All the XRD peaks of the Al04 oxide can be indexed on the basis of an orthorhombic unit cell of $CaFe_2O_4$-type structure (SG: *Pnma*) with relationships of the lattice vectors of the orthorhombic subcell and the monoclinic supercell given by the following matrix relation:

$$(a_m, b_m, c_m) = (a_o, b_o, c_o) \begin{bmatrix} 1 & 0 & 0 \\ 2 & 0 & -3 \\ 0 & 1 & 0 \end{bmatrix}$$

In order to conclude definitively about this change of symmetry, electron diffraction investigation of Al04 sample has been performed and the reciprocal space has been reconstructed. An orthorhombic unit cell can be easily identified and the unit cell parameters $a \approx 8.9$ Å, $b \approx 2.8$ Å and $c \approx 11.3$ Å are close to those found for $CaFe_2O_4$-type structure [14, 21]. The electron diffraction pattern corresponding to the [-1 0 0] and [-1 0 1] zone axis are represented on Figure 2. No general reflection condition was observed which implies a P Bravais lattice. On the [-1 0 0] zone axis pattern, the reflection condition k + l = 2n is consistent with an n glide plane. The arrow on the [-1 0 1] zone axis pattern, obtained with a precession angle of 2.5°, shows the absence of the 010 reflection in accordance with the Pnma space group. In addition to these clear reflections, weak diffuse lines are visible. Their presence indicates a tendency to additional local ordering.

The XRD diagrams of $Ca_{0.66}Mn_{2-x}Al_xO_4$ compositions (x=0, 0.2, 0.4, 0.47) have been represented on Figures 3 and S3. By decreasing the Al content from x=0.4 to x=0.2 (noted Al02), the XRD superstructure lines of the monoclinic unit cell are still absent (Figure 3) and all the peaks can also be indexed on the basis of an orthorhombic unit cell with the *Pnma* space group. In contrast, by increasing the Al content from x=0.4 to x=0.47 a small shoulder on the right of the main peak (marked with a star on Figure 3 and S3) is seen corresponding to the main XRD line of $Ca_2(Mn,Al)_2O_5$ Brownmillerite-type phase [8]. Only the x=0.47 composition is not single phase. All these results allow the definitive conclusion that the $Ca_{0.66}Mn_{1.6}Al_{0.4}O_4$ oxide adopts the $CaFe_2O_4$-type framework with a large content of Ca vacancies and that Al^{3+} substitution suppresses the 1-2-type long range ordering of one vacancy and two calcium cations in $CaMn_3O_6$.

Rietveld refinements of powder XRD data of $Ca_{0.66}Mn_{2-x}Al_xO_4$ compositions (x=0, 0.2, 0.4) have been carried out and are represented on Figures S2 and 4a-b respectively. The atomic positions, the unit cell parameters and volume are reported on Table 1. In the $CaFe_2O_4$-type network, two various crystallographic sites for transition metals at (x, 1/4, z) can be identified. In a first structural hypothesis, one considers that Al^{3+} ions are distributed over the two transition metal crystallographic sites. Al occupancies for these two atomic positions have been refined (Tables S1 and S2) considering that the atomic number (Z) of Mn (Z=25) and Al (Z=13) are very different (see Tables S2a-b). For Al02 and Al04 compounds, the occupancies are higher in the Mn2 sites and are equal to 0.144(1) and 0.246(1) respectively. Moreover, the analysis of Mn/Al-O bond distances shows for both these compositions two very different local environments for Mn/Al atoms which do not vary versus the Al concentration. The $Mn2O_6$ octahedra, where Al atoms are mainly located, are the most regular with Mn2-O bond distances between 1.90 Å and 1.98 Å. The <Δ> average of differences between the Mn2-O distance and the average distance is small and equal to 0.03 Å (Tables S2a-b). The average Mn/Al-O bond distance equal to 1.94 Å is in good agreement with Mn^{4+} (r[6] = 0.53 Å) or Al^{3+} (r[6] = 0.54 Å) ionic radii. However, the second octahedra corresponding to the Mn1 atomic position is highly elongated with 4 equatorial Mn-O bond distances around 1.92 Å and two apical one's around 2.22 Å and 2.30 Å regardless of the chemical composition. The <Δ> average of differences between the Mn/Al -O distances and the average Mn/Al-O distance is larger and equal to 0.15 Å (Tables S2a-b) . If these distorted octahedra are the signature of a Mn^{3+} Jahn-Teller ion , the location of Al atoms in these sites is highly improbable because of Al^{3+} smaller ionic radius and its isotropic character. Therefore, a second structural hypothesis was taken into account where all Al atoms occupy partially only the Mn2 sites (Tables 2a-b and 3a-b). The refinements are correct with rather low reliability factors (Bragg factors equal to 7.0% and 8.8% for Al04 and Al02 samples respectively). They are close to those obtained for the first structural hypothesis (in this case, Bragg factors equal to 6.4% and 8.7% for Al04 and Al02 samples respectively). The Mn/Al-O bond distances are not strongly affected by this new Al distribution. The comparison between the Mn1 site and the Mn^{3+} local environments in $Ca_{0.75}Mn_2O_4$ [21] (SG : *Pnma*, 1 Mn^{3+} and 1 $Mn^{3.5+}$) oxides shows that the distortion induced by the Jahn-Teller effect is almost always identical in these 1D tunnel frameworks with four short

distances around 1.92 Å and two longer one's around 2.20 Å and 2.30 Å . The other $Mn^{3.5+}$ site in $Ca_{0.75}Mn_2O_4$ [21] is also larger and more distorted (distances varying from 1.92 Å to 2.08 Å) than the Mn2 site with a random distribution of Mn^{4+} and Al^{3+} (distances from 1.90 Å to 1.98 Å), showing a strong increase of the Mn valence state in the Mn2 site. On the basis of these latter refinements, the following chemical formulae can be written: $Ca_{0.66}(Mn^{3+})(Mn^{4+}_{0.67}Mn^{3+}_{0.33})O_4$, $Ca_{0.66}(Mn^{3+})(Mn^{4+}_{0.67}Mn^{3+}_{0.13}Al_{0.2})O_4$ and $Ca_{0.66}(Mn^{3+}_{0.93}Mn^{4+}_{0.07})(Mn^{4+}_{0.6}Al_{0.4})O_4$ for undoped, Al02 and Al04 samples respectively. In site 1, the Mn1 valence state remains equal to +3 for x=0 and x=0.2, then increases to +3.07 for x=0.4. However, in site 2, The Mn valence state increases regularly from +3.66 (x=0) to +3.84 (x=0.2), then +4 (x=0.4). In the x=0.33 target composition, site 1 would be fully occupied by Mn^{3+} and site2 would contain 2/3 of Mn^{4+} and 1/3 of Al^{3+}. The two various structures corresponding to $CaMn_3O_6$=$Ca_{0.66}Mn_2O_4$ (monoclinic symmetry, 2 $Mn^{(4-\delta)+}$ sites and 4 $Mn^{(3+\delta)+}$) and $Ca_{0.66}(Mn_{2-x}Al_x)O_4$ (x=0.2 and 0.4, orthorhombic symmetry, 1 $Mn^{(3+\delta)+}$ site and 1 $Mn^{(4-\delta)+}$ site) are represented in Figure 5. When Al is substituted in $Ca_{0.66}Mn_{2-x}Al_xO_4$, the 1-2-type long range ordering of one vacancy and two calcium cations in $CaMn_3O_6$ is suppressed. In the Al-substituted phases, the building blocks of the framework correspond to two rutile double chains with trivalent Mn cations in one site and in the other one's tetravalent and trivalent cations arranged in a chessboard pattern in relation with the $CaFe_2O_4$ network.

A full pattern profile matching of the powder XRD diagram of x=0.47 composition shows the unit cell parameters and volume (*a* = 8.963(1) Å, *b* = 2.825(3) Å, *c* = 11.281(2) Å, V = 285.70(7) $Å^3$) are close to what we found for the x=0.4 (Al04) compound (*a* = 8.9535(2) Å, *b* = 2.8239(1) Å, *c* = 11.2802(3) Å, V = 285.21(1) $Å^3$). Further, the variation of unit cell parameters and volume represented in Figure 6 shows a strong decrease of all these parameters for low Al content which tends to an asymptotic value for x=0.4 around this Al solubility limit. The decrease of the unit cell parameters is in good agreement with the lower ionic radius of Al^{3+}, substituted for Mn^{3+} in site 2 where Mn^{4+} ions are mainly localized. As all the Al atoms replace the Mn^{3+} ions located in the Mn2 site, the x(Al) content reaches the 0.33 value and the cell parameters tend to a plateau. For x > 0.33, a few Mn^{4+} ions can be stabilized in the Mn1 site but the framework does not support any excess of Mn^{4+} in this highly

distorted site and the Al solubility limit is reached for 0.4 < x < 0.47 for which the limit Mn^{4+} rate in Mn1 site is between 0.07 and 0.14.

Magnetic properties

Figure 7 shows the temperature dependences of the magnetic susceptibilities on a log scale from T = 4 K to T = 400 K for a magnetic field H of 10 kOe corresponding to x= 0, 0.2 and 0.4 compositions. The temperature dependence of the magnetic susceptibility in a linear scale for $CaMn_3O_6$ (i.e. $Ca_{2/3}Mn_{2-x}Al_xO_4$ (x=0)) compound is zoomed in the inset of figure 7 for clarity. An anti-ferromagnetic character with a local maximum at T_N around 50 K defined for the temperature at which a deviation between the zero field cooled (ZFC) and the field cooled (FC) data occurs is seen for $CaMn_3O_6$. The shape of its magnetic behavior and its ordering temperature range are both similar to those observed in hollandite related compounds made of double chains (zigzag chains) formed by edge-sharing MnO_6 octahedra for $Ba_{1.2}Mn_8O_{16}$ [25] and for $K_{1.6}Mn_8O_{16}$ [26]. In a first assumption, a Curie-Weiss law analysis on a temperature range from 250 K to 400 K further supports the antiferromagnetic ground state with a Weiss temperature θ around -600 K (Figure S4). The estimated paramagnetic moment (μ_{eff}) is found to be 5.00 μ_B/Mn. Interestingly, it is in the same range of order than the one reported by Glaunsinger *et al.* [27] but larger than that expected for an ionic model corresponding to 4.58 μ_B/Mn. These deviations from ideality show that the magnetic behavior in this temperature range cannot be understood in terms of paramagnetism of isolated ions that might explain the reported discrepancies [17, 25]. Two main reasons could be considered to understand these differences. The first one is that magnetic clusters likely occur in relation to the structural analysis showing $Mn^{(4-\delta)+}O_6$ octahedra associated into groups and separated by two $Mn^{(3+\delta)+}O_6$ octahedra in connection to the calcium 1-2-type ordering. This was previously observed in the literature for $La_{0.7}Ca_{0.3}MnO_3$ towards the paramagnetic to ferromagnetic transition [26] and for Bi-manganites 3:1 Mn^{3+}/Mn^{4+} charge ordering compounds [27]. As expected from chains in this structure [30] the considerable $|\theta/T_N| \approx 30$ ratio indicates a frustration effect associated with the small thermal hysteresis occurring before 50K between the ZFC and the FC data and can further support this hypothesis. Magnetic susceptibility measurements performed at much higher temperatures to reach the ionic

paramagnetic state are required [31]. The second one is the lack of the consideration of the electron correlations and especially of the possible direct overlapping of the t_{2g} orbitals in the double chains formed by edge-sharing MnO_6 octahedra. Thus the data were also fitted to the Curie–Weiss law with a temperature independent term, $\chi(T) = \chi_0 + C/(T - \theta)$ as proposed in the hollandite $Ba_{1.2}Mn_8O_{16}$ [25]. The temperature range from 150 and to 390 K used for the fit was deduced from different tests extracting a better agreement factor. The fit results with their quality factors are shown in Table 3 with those also found for the composition with aluminum. The estimated paramagnetic moment μ_{eff} is now smaller than that expected for an ionic model which is indicative of the splitting in between localized and delocalized electrons. As the Al content increases, the anti-ferromagnetic character decreases: the low temperature part of the magnetic susceptibilities curves does not show any maximum for both samples and the fitted θ Weiss temperatures are found around -300 K for Al02 and around -200 K for Al04 within an only Curie Weiss law model. The estimated effective paramagnetic moments decrease with aluminium content from μ_{eff} = 4.30 μ_B/Mn to μ_{eff} = 4.22 μ_B/Mn and become smaller than the ones' expected for an ionic model with 4.54 μ_B/Mn for Al02 and 4.50 μ_B/Mn for Al04 respectively. If one considers the Curie–Weiss law with a temperature independent term, a significant content of electrons would still be delocalized within the double chains despite the presence of $3s^0$ aluminium ion and the Weiss temperatures are still found to be negative, supporting antiferromagnetic super exchange interactions. However, their absolute values are a better match with the temperature range for which we are fitting the data. To gain a better understanding of the magnetization change with Al^{3+} substitution at temperatures lower than 50K, isothermal field-dependent magnetization studies were carried out. Figure 8 shows the net increase in hysteresis field with Al^{3+} substitution at T = 4 K at the bottom of a linear behavior related to antiferromagnetic interactions.

In our 1D-tunnel network, which derives from $CaFe_2O_4$-type like in the manganese hollandites structures, the ordering temperature of undoped sample occurs below 50 K with a magnetic state that is fundamentally antiferromagnetic. When Al^{3+} is introduced, the ordering temperatures defined by the minimum on the derivative curves remain at 50 $\pm$ 5 K. It suggests that the magnetic ground state is controlled by the magnetic exchange interaction within the double chains and that the deviation from one composition to another originated from the inter-chain magnetic

exchanges. From Hartree–Fock calculation on a multi-band Mn 3d–O 2p lattice model,[32] Fukuzawa and co-workers propose that all Mn^{3+}-O-Mn^{4+} , Mn^{3+}-O-Mn^{3+}, and Mn^{4+}-O-Mn^{4+} super-exchange interactions are ferromagnetic within the double chain in this charge ordering pattern. They are reinforced by the 90° ferromagnetic interactions but the direct exchange through the t_{2g}, overlapping within the double chain, needs also to be considered. This is correlated to the paramagnetic temperature independent term (if it is to be taken into account). In contrast the inter-chain magnetic exchanges at 180° angle configuration are antiferromagnetic. However, they are weakened due to the low Mn–O–Mn bond angles in this structure (Table 4) that is much smaller than the required ideal 180° angle. As aluminum content increases, the local charge ordering may be preserved and the Mn-O-Mn interchain angles are not significantly changed. But the Mn^{4+}/Mn^{3+} ratio increases. Because the superexchange that involves ½ filled e_g orbitals (i.e. 180° Mn^{3+}-O-Mn^{3+} interactions) is much stronger than the corresponding interaction of ½ filled t_{2g} orbital (i.e. 180° Mn^{4+}-O-Mn^{4+} interactions), aluminum content increase results in a weakening of the global antiferromagnetic long range interactions in good agreement with the variation of magnetic properties with Al content illustrated in Figures 7 and 8. Thus, $Ca_{0.66}Mn_{2-x}Al_xO_4$ compounds are likely canted antiferromagnets. Beyond our hypothesis, joint temperature dependence powder neutron diffraction and/or density functional theory calculations are needed to extract the magnetic ground state for which a spin glass behavior cannot be excluded even if the thermal hysteresis between the ZFC and FC data for $Ca_{0.66}Mn_{1.6}Al_{0.4}O_4$ is poor.

Redox properties and correlation with structural features

To illustrate the redox cycling properties of these complex oxides, thermogravimetric analyses (TGA) under reducing atmosphere (Ar/5% H_2) were carried out. Redox cycling behavior of $Ca_{0,66}Mn_{1,6}Al_{0,4}O_4$ is presented on Figure 9. The weight loss percentage $\Delta m/m$, the exchanged oxygen atoms per manganese ΔO starting from $Ca_{0.66}Mn_{1.6}Al_{0.4}O_4$ chemical formulae and the temperature of reduction/oxidation are reported in Table 5. The first reduction occurs mainly between 325 °C and 640 °C. The large content of exchanged oxygen atoms around 0.7 per manganese corresponds exactly to the total reduction of $Mn^{4+/3+}$ into Mn^{2+}. The re-

oxidation starting at 150 °C is slower and occurs through different oxidation steps with a first plateau at 450 °C up to 700 °C then a second plateau starts at 750 °C. However the final state expected for the right ΔO value (*i.e.* for complete reoxidation) is not yet reached at 800 °C in these oxygen partial pressure and kinetic conditions. Finally the successive reduction occurs roughly in the same temperature range than the first one and the exchanged oxygen content corresponds to the rate obtained after the re-oxidation. However, the slope of the second reduction is clearly higher than the first one. The powder XRD analysis of the reduced phase containing only Mn^{2+} reveals the stabilization of a pure rocksalt-type structure whatever the composition of the oxidized sample (x = 0, 0.2 and 0.4, see Figure 10). Moreover the variation of refined cell parameter versus Al^{3+} or Mn^{2+} contents (Figure S5) follows a Vegard law (Figure 11). Regardless of the Mn or Al amounts, a complete solid solution forming a rocksalt-type network is obtained despite the large difference of cations' ionic radii, 6-fold coordinated to oxygen ($r(Ca^{2+})$=1.0 Å, $r(Mn^{2+})$=0.83 Å, $r(Al^{3+})$=0.53 Å). The re-oxidation up to 850 °C is slower but leads to the stabilization of the starting oxide (same unit cell parameters and composition). In-situ powder XRD experiments during the oxidation of the rocksalt-type framework show the formation of amorphous phases starting from 500 °C corresponding to the first plateau on the TGA curve up to 850 °C as the $CaFe_2O_4$-type structure is stabilized. Reduction process occurs systematically in the same temperature range for both the starting oxide and the cycled material. During oxidation, the smaller ionic size of Al^{3+} forces a definite distribution of the manganese ions into the two crystallographic sites depending on their valencies which should explain why the reduction takes place in the same temperature range after several cycles. The change of reduction slopes should be due to the various distributions of Al^{3+} substituted for Mn^{4+} in the same site (homogeneity being better after cycling) which could affect the iono-covalence of Mn^{4+}-O chemical bonding and its capability to be reduced. One should notice that the morphology of particles can also evolve when cycling.

The comparison of TGA curves and their derivatives obtained during the reduction processes of the x = 0, 0.2 and 0.4 compositions are represented in Figure 12. For the x = 0 compound, starting at 250 °C, two reduction phenomena can be clearly identified and are separated by a pseudo plateau centered around 420 °C which corresponds to the local maximum of the derivative curve. The weight loss for

the first phenomena is equivalent to that of the second one. In a first approximation, the description of the monoclinic unit cell of $CaMn_3O_6$ on the basis of an orthorhombic unit cell ('$Ca_{0.66}Mn_2O_4$') leads to the identification of two Mn sites with the same multiplicity and corresponding to +3.66 and +3 valence states respectively. Therefore, we propose that the first reduction at lower temperature should correspond to the mixed valence state $Mn^{4+/3+}$: at the first inflexion point Mn^{4+} is fully reduced into Mn^{3+} and at the first local maximum of the derivative curve, the average valency reaches the value of $Mn^{2.66+}$ (*i.e.* 66% of Mn^{3+} and 34% of Mn^{2+}). The reduction of Al-substituted phases shifts to higher temperatures and the local maxima of the derivative curves, which are much more attenuated, appear around 470°C for Al02 and Al04 samples. Moreover, Mn^{4+} being located at the same atomic position as Al^{3+} in one specific double chain, the Mn-O chemical bonding in this site becomes more covalent as Al content increases due to a less distorted site and shorter bond distances. Thus, the reduction phenomenon of the Al-substituted phases occurs at higher temperature. However, the thermal stability under air of Al-substituted $Ca_{0.66}Mn_{2-x}Al_xO_4$ oxides remains the same as the $Ca_{0.66}Mn_2O_4$ un-substituted compound at T < 900 °C. That is why, in order to increase or decrease the Mn^{4+} contents, other compositions with slightly lower and larger Ca contents have been attempted. A target corresponding to $Ca_{0.6}Mn_{1.6}Al_{0.4}O_4$ composition (Figure 13) leads to a phase mixture with $CaFe_2O_4$-type framework and Brownmillerite-type structure ($Ca_2(Mn,Al)_2O_5$, SG: *Imma*) [8]. However the $Ca_{0.7}Mn_{1.8}Al_{0.2}O_4$ composition is pure and adopts the $CaFe_2O_4$-type network (Figure 13). It is noteworthy to mention the slight increase of *a* and *c* unit cell parameters (Table 1) compared to those of $Ca_{0.66}Mn_{1.8}Al_{0.2}O_4$ oxide with the shift at low 2θ angles of (002), (102) and (200) diffraction lines (Figures 13 and S6). The Ca vacancy rate equal to y=1/3 is the upper limit to be reached in the $Ca_{1-y}Mn_{2-x}Al_xO_4$ solid solution. While the Mn average oxidation state of $CaMn_3O_6$ and $Ca_{0.7}Mn_{1.8}Al_{0.2}O_4$ oxides is the same and equal to +3.33, the Mn average valence state slightly increases with Al amount for the $Ca_{0.66}Mn_{2-x}Al_xO_4$ composition up to +3.42 for x=0.4.

Conclusion

The Al substitution in the $CaMn_3O_6$ 1D-tunnel structure (SG: *P21/a*) allows the stabilization the $CaFe_2O_4$-type structure with a higher symmetry (SG: *Pnma*) and to tune the Mn valence state in the two atomic positions (x, ¼, z). The unit cell parameters of the $Ca_{0.66}Mn_{2-x}Al_xO_4$ solid solution strongly decrease with Al content increase and tend to an asymptotic value around x = 0.33. The solubility limit is reached for $0.4 < x < 0.47$. The two Mn sites are clearly different. The first one, Mn1, is highly anisotropic with four short bond lengths and two longer one's corresponding mainly to Mn^{3+} ($3d^4$) as Jahn-Teller ion. The second one Mn2 is smaller, more isotropic and partially occupied by Al^{3+} ions. For x = 0.33, the second site is occupied by 2/3 of Mn^{4+} and 1/3 Al^{3+} whereas 100% of Mn^{3+} are located in the first site. Magnetic properties follow this Mn valence distribution due to the Al site occupancy and show a modification of the balance between ferromagnetic and antiferromagnetic interactions, the inter-chain long range antiferromagnetic interactions being strongly weakened when aluminium content increases. The Al substitution for Mn sites in $CaMn_3O_6$ network contributes to the modification of the long range Mn charge ordering, which leads to change the symmetry of the unit cell with the disappearance of the Ca ordering. The reduction of Al-substituted phases starts at higher temperature (T = 350 °C) than the $CaMn_3O_6$ oxide (ΔT = +50 °C), confirming the increase of the Mn-O bond covalence with the Al substitution. The reduced phases correspond to a perfect solid solution, stabilizing Al^{3+}, Mn^{2+} and Ca^{2+} (which have very different ionic sizes) in a rocksalt-type structure. The two rutile double chains in the $CaFe_2O_4$-type structure, involving two various valence states for Mn, are clearly related to the rocksalt-type structure and should explain the two reduction phenomena observed at different temperatures. If the oxidation of reduced phases takes place at lower temperatures (T = 150 °C), the phenomenon is slower than the reduction process and amorphous phases appear before the stabilization of $Ca_{0.66}Mn_{2-x}Al_xO_4$ solid solution at T = 850 °C. The very good cyclability of this system should be associated to the presence of Al^{3+} which substitutes Mn^{4+} in the same atomic positions, thus playing the role of pillar where the Mn-O-Mn interactions involving two rutile double chains can easily develop.

References

[1] Funabiki. M., Yamada. T., Kayano. K. *Catal. Today* **1991**, *10*, 33

[2] Kaspar, J.; Fornasiero, P.; Hickey, N. *Catal. Today* **2003**, *77*, 419.

[3] Trovarelli. A, "Catalysis by Ceria and related materials" Imperial College Press, **2002**

[4] Reddy. B.M, Reddy. G.K., Ganesh. I., Ferreira. J.M.F. *Catal. Lett.* **2009**, *130*, 227

[5] Achary. S.N, Kali. S.K, Kulkarni. N.K, Krishna. P.S.R, Shinde. A.B, Tyagi, A.K. *Chem. Mater.***2009**, *21*, 5848.

[6] Abel. J, Lamirand-Majimel. M, Majimel. J, Bellières-Baca. V, Harlé. V, André. G, Prestipino. C, Figueroa. S, Durand. E, Demourgues. A. *Dalton Trans.* **2014**, 43, 15183-15191.

[7] Yamaguchi H, Yamada A, Hiromoto U. *Phys. Rev. B*. **1998**, 58(1) 8–11.

[8] Motohashi T, Hirano Y, Masubuchi Y, Oshima K, Setoyama T, Kikkawa S. *Chem.Mater.* **2013**,25,372–377.

[9] Poeppelmeier KR, Leonowicz ME, Scanlon JC, Longo JM, Yelon B. *J.Sol.Stat.Chem* **1982**,79,71–79.

[10] Varela A, de Dios S, Parras M, Hernando M.,Fernández-Díaz M T. Landa-Cánovas, A. R. González-Calbet, J. M. *JACS*. **2009**,131(24):8660–8668.

[11] Negas T, Roth RS. *J.Sol.Stat.Chem*. **1970**,1:409–418.

[12] Horowitz H.S and Longo J.M. *Mater. Res. Bull.*. **1978**,13:1359–1369.

[13] Yamanaka T, Uchida a., Nakamoto Y. *Am. Mineral*. **2008**, 93(11-12),1874–1881.

[14] Zouari S., Ranno L., Cheikh-Rouhou A., Pernet M., Strobel P. *J. Mater. Chem*. **2003**,13(4):951–956.

[15] Zouari S, Ranno L, Cheikh-Rouhou A, Isnard O., Pernet M., Wolfers M., Strobel P., .*J.Alloys.Compd*. **2003**,353(1-2), 5–11.

[16] Ling. C.D, Neumeier. J.J, Argyriou. D.N. *J. Sol. Stat. Chem.* **2001**, 160, 167-173.

[17] Hadermann J, Abakumov A.M, Gillie L.J, Martin C. *Chem. Mater.* **2006**, (9),5530–5536.

[18] Tsipis E, Pivak Y, Waerenborgh J, Kolotygin V, Viskup A, Kharton V. *Sol. Stat Ion*. **2007**,178(25-26):1428–1436.

[19] Sławiński W, Przeniosło R, Sosnowska I, *J. Sol. Stat. Chem*. **2013**,198,392–398

[20] Barrier N, Michel C, Maignan A., Hervieu M, Raveau B. *J.Mater.Chem*. **2005**,15, 386-393.

[21] Yang T, Croft M, Ignatov A, Nowik I, Cong R, Greenblatt M. *Chem.Mater.* **2010**,22,5876–5886.

[22] Chick L., Pederson L., Maupin G., Bates J., Thomas L., Exarhos GJ. *Mater. Lett*. **1990**,10, (1,2),6–12.

[23] Deshpande K., Mukasyan A., Varma A. *J. Am Ceram. Soc.* **2003**, 54,1149–1154.

[24] Epherre R., Duguet E., Mornet S., Pollert E., Louguet S.,Lecommandoux S., Schatz C., Goglio G. *J. Mater. Chem*. **2011**, 21, 4393-4401.

[25] Ishiwata S., Bos J.W.G., Huang Q. and Cava R.J. *J. Phys.: Condens. Matter* **2006**, 18 3745–3752

[26] Kuwabara T., Isobe M., Gotou H., Yaga T., Nishio-Hamane D. and Ueda Y. *J. Phys. Soc. Jap.* **2012,** 81, 104701.

[27] Glaunsinger. W.S, Horowitz. H.S, Longo. J.M, Chang. A. *J. Sol. Stat. Chem.* **1980**, 35, 187-191. *

[28] Anil Kumar. P.S, Joy. P.A, Date. S. K. *J. Phys.: Condens. Matter*.**1998**, 10, 269–275

[29] Toulemonde. O, Skovsen. I, Mesguich. F, Gaudin. E. *Sol. Stat. Sci.* **2008**, 10(4), 476-480

[30] Q. Liu, D. Sallagoity, M. Josse, and O. Toulemonde *Inorg. Chem.* **2013**, 52, 7853−7861],

[31] J.E. Greedan, N.P. Raju, I.J. Davidson *J. Sol. Stat. Chem*. **1997**, 128, 209-214

[32] M. Fukuzawa, D. Ootsuki, and T. Mizokawa *J. Phys. Soc. of Jap*. **2013**, 82 074708

Figure captions

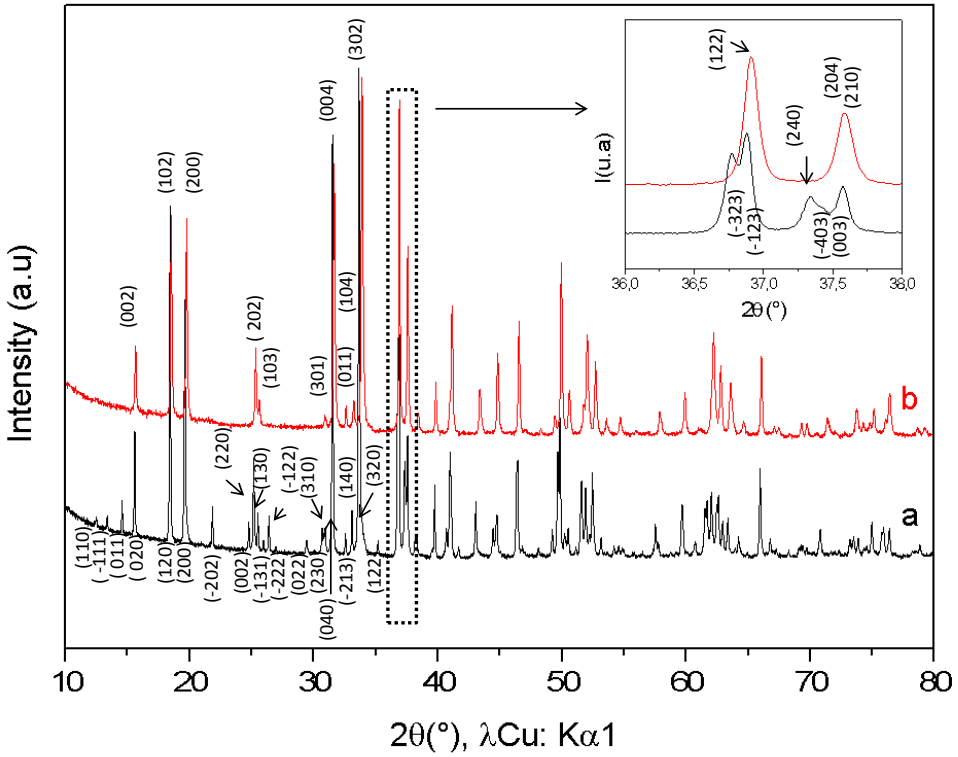

Figure 1: X-ray powder diffraction patterns of a) $CaMn_3O_6$=$Ca_{0.66}Mn_2O_4$ (monoclinic unit cell, SG: $P2_1/a$) and b) $Ca_{0.66}Mn_{1.6}Al_{0.4}O_4$ (orthorhombic unit cell, SG: Pnma) compounds. (hkl) indexations at low 2Θ angles are mentioned.

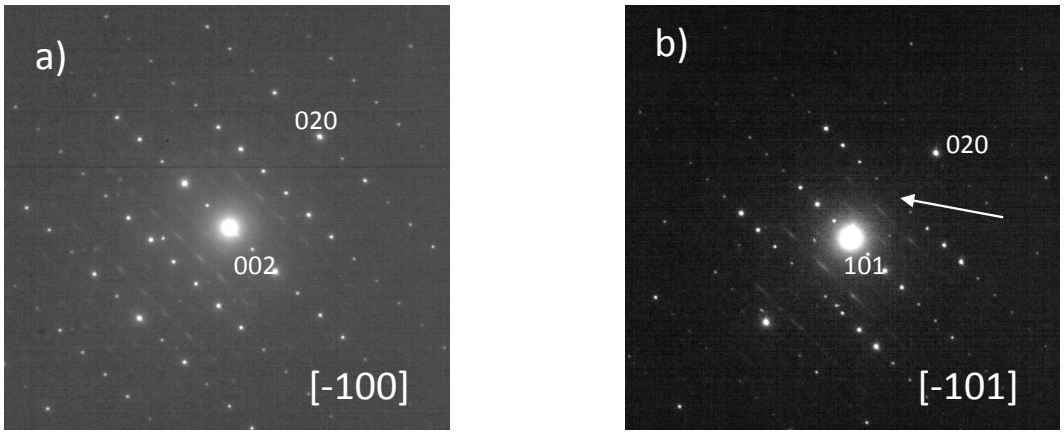

Figure 2: Electron diffraction patterns corresponding to a) [-100] and b) [-101] zone axis for $Ca_{0.66}Mn_{1.6}Al_{0.4}O_4$ oxide. The condition 0kl k+l= 2n is observed on the [-100] zone axis pattern. The arrow indicates the absence of the 010 reflection consistent with the *Pnma* space group.

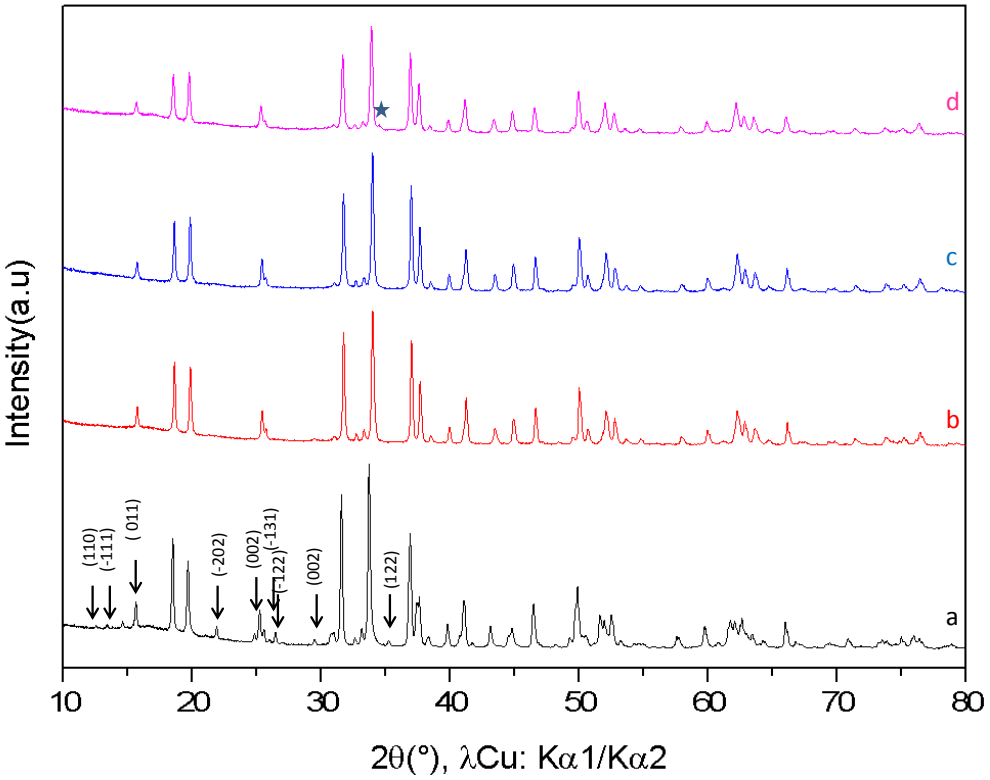

Figure 3: X-ray powder diffraction patterns of $Ca_{0,66}Mn_{2-x}Al_xO_4$ ($0<x\leq0.47$) a) x=0 , b) x=0.2, c) x=0.4 and d) x=0.47. For x=0.47, the major diffraction peak of the impurity phase (Brownmillerite-type phase) is marked by a star.

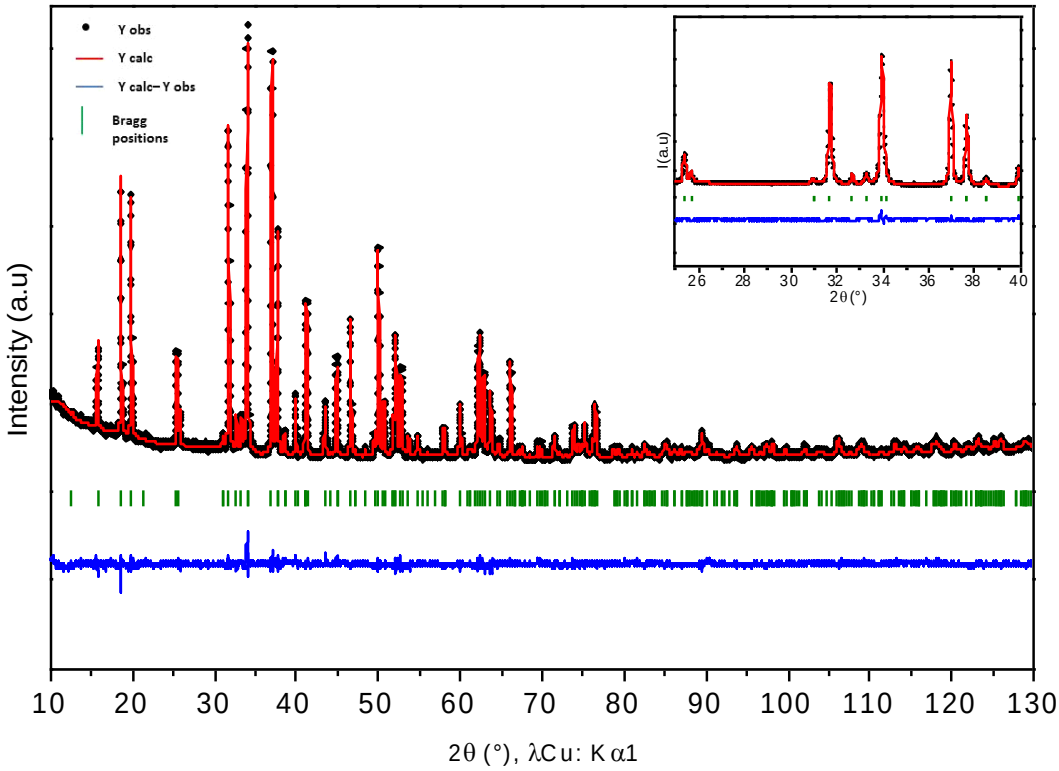

Figure 4a: Rietveld refinement of X-ray powder diffraction patterns of $Ca_{0.66}Mn_{1.6}Al_{0.4}O_4$ compound. Calculated (in red), observed (in black), difference (in blue) patterns are represented. Bragg peaks (in green) are mentioned. Structural hypothesis: all Al^{3+} ions are located in site 2 (Mn^{4+}).

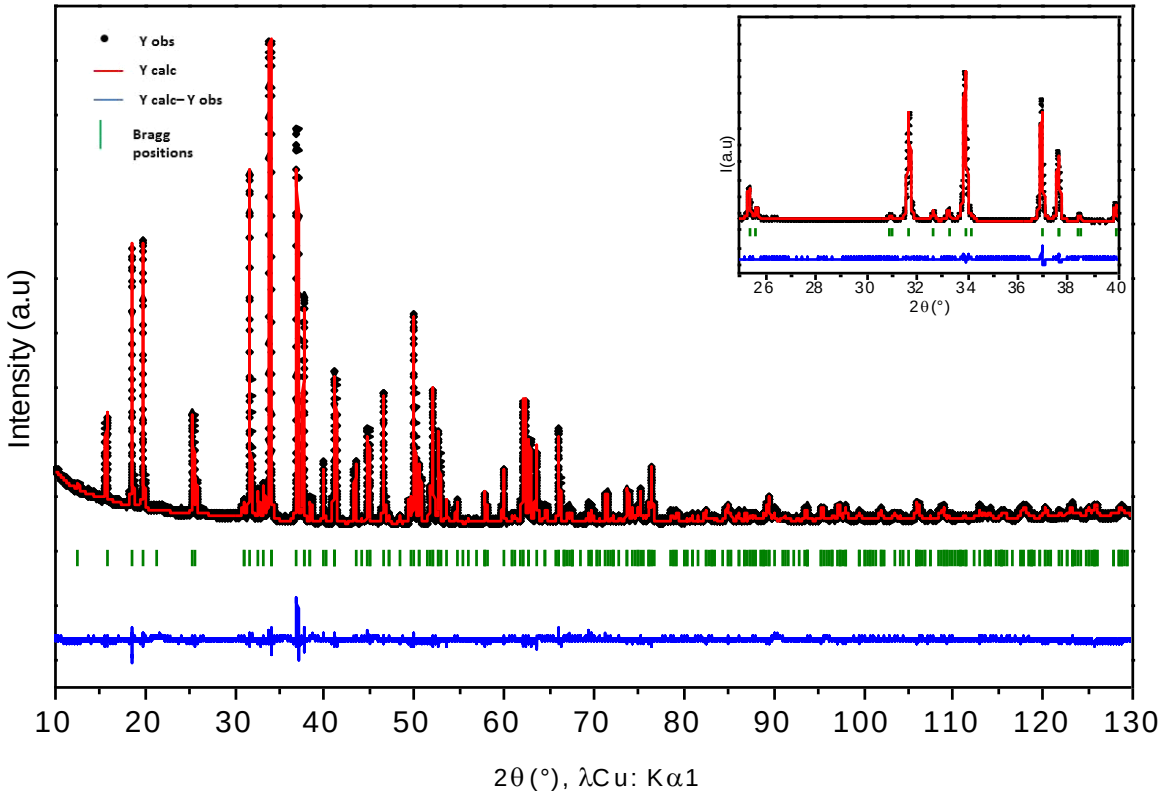

Figure 4b: Rietveld refinement of X-ray powder diffraction patterns of $Ca_{0.66}Mn_{1.8}Al_{0.2}O_4$ compound. Calculated (in red), observed (in black), difference (in blue) patterns are represented. Bragg peaks (in green) are mentioned. Structural hypothesis: all Al^{3+} ions are located in site 2 (Mn^{4+}).

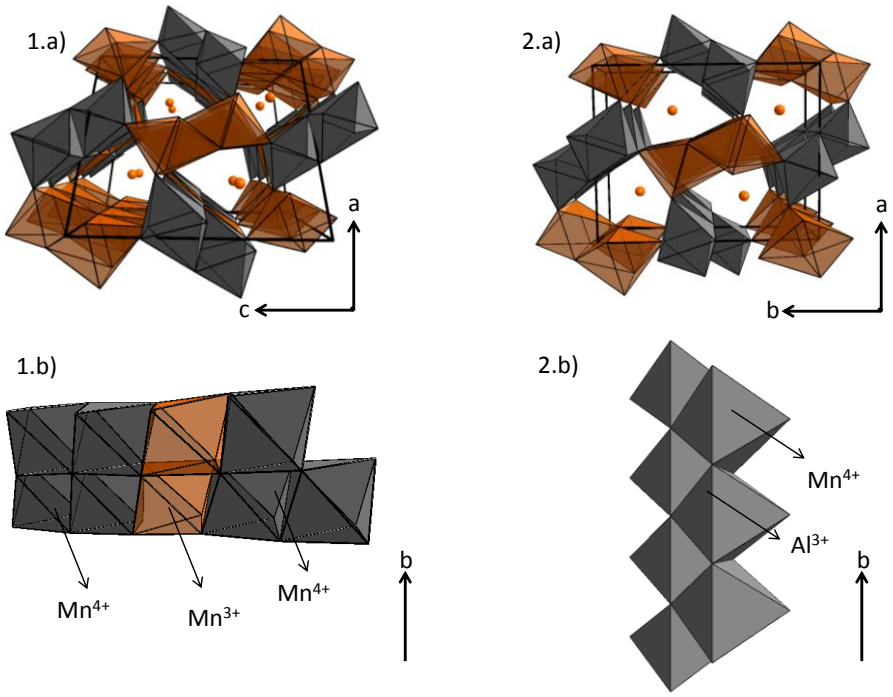

Figure 5: Structures representation of 1.a) $CaMn_3O_6$=$Ca_{0.66}Mn_2O_4$ (monoclinic unit cell, SG: *P21/a*, 6 Mn sites: 4Mn^{3+} in orange and 2 Mn^{4+} in grey) and 2.a) $Ca_{0.66}Mn_{2-x}Al_xO_4$ (x = 0.2 and 0.4) (orthorhombic unit cell, SG: *Pnma*, 2Mn sites: 1 Mn^{3+} in orange and 1 Mn^{4+} / Al^{3+} in grey) compounds. The linkage of double chains viewed perpendicular to *b* axis is presented in Fig 5.1.b for $Ca_{0.66}Mn_2O_4$ and in Fig. 5.2.b for $Ca_{0.66}Mn_{2-x}Al_xO_4$ (x=0.33: all Mn^{3+} are substituted by Al^{3+} ions).

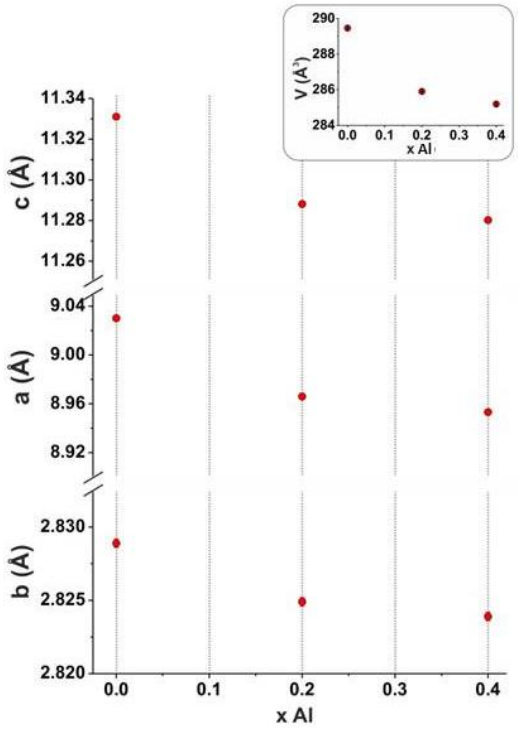

Figure 6: Unit cell parameters and volume variation of $Ca_{0.66}Mn_{2-x}Al_xO_4$ ($0<x\leq0.40$) compounds (orthorhombic unit cell, SG: *Pnma*).

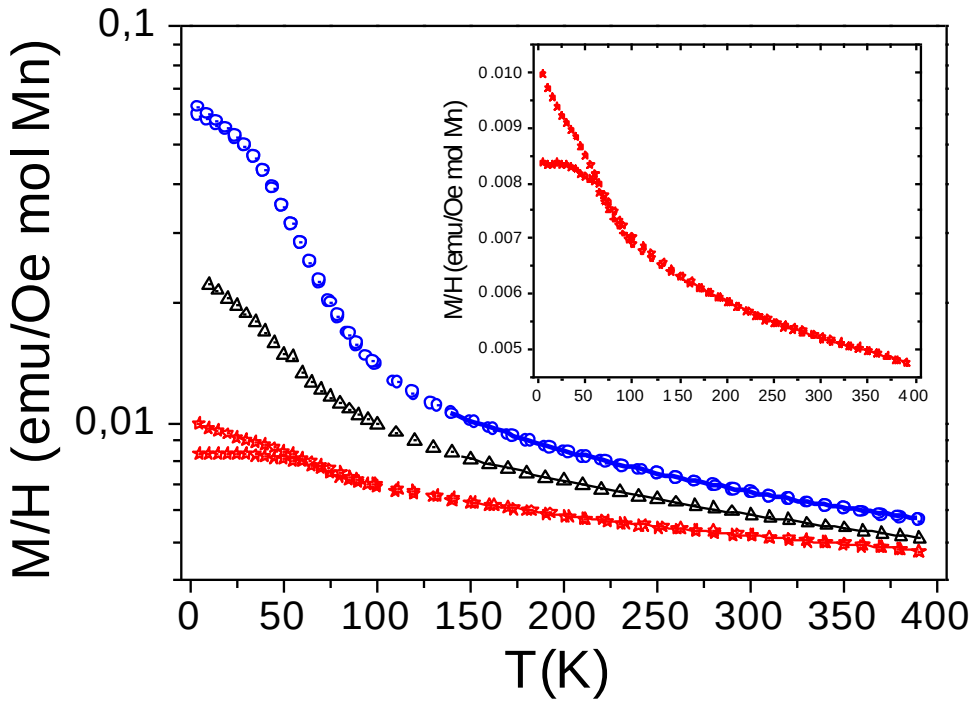

Figure 7: Comparison of the temperature dependence of magnetization curve per mole of Mn for $Ca_{0.66}Mn_2O_4$ (in red) , $Ca_{0.66}Mn_{1.8}Al_{0.2}O_4$ (in black) and $Ca_{0.66}Mn_{1.6}Al_{0.4}O_4$ (in blue) compounds (recorded with a magnetic field of 10 KOe). The solid line represent Curie–Weiss paramagnetism law obtained by fitting the data with a temperature independent term, $\chi(T) = \chi_0 + C/(T - \vartheta)$

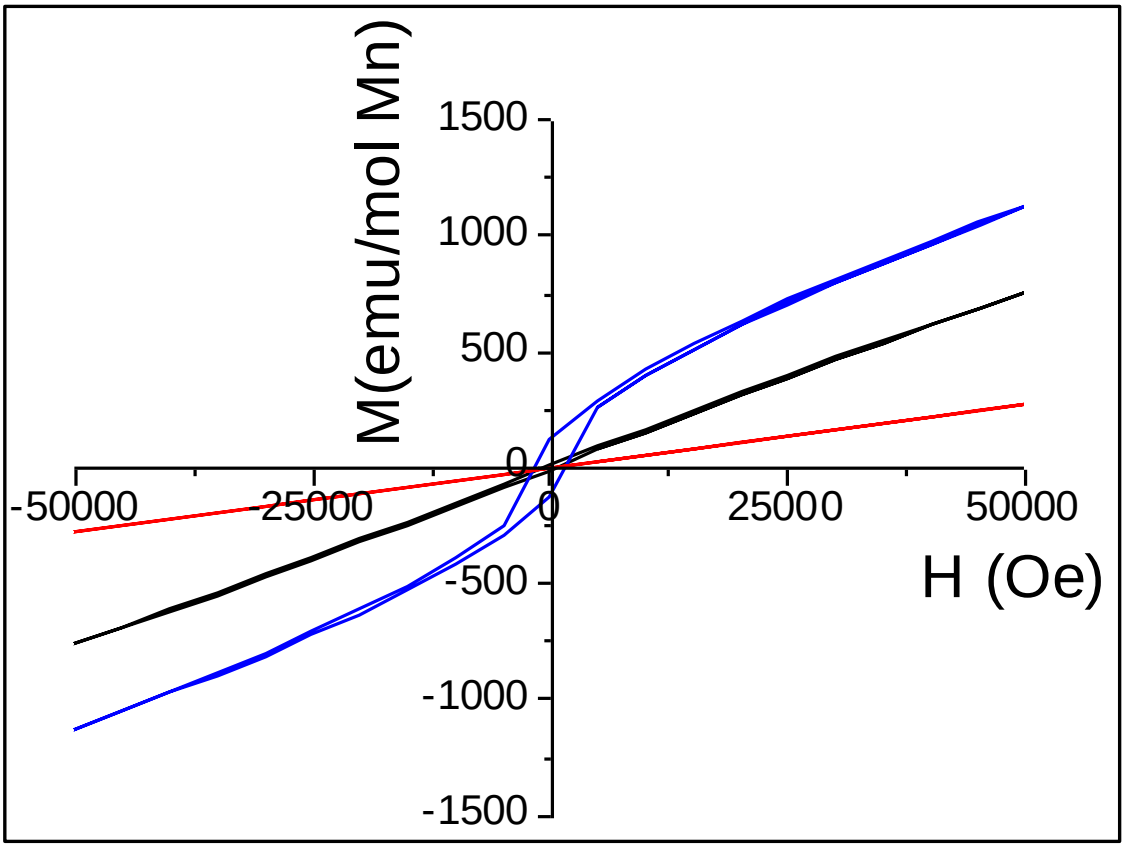

Figure 8: Comparison of field dependence of magnetization curve per mole of Mn for $Ca_{0.66}Mn_2O_4$ (in red), $Ca_{0.66}Mn_{1.8}Al_{0.2}O_4$ (in black) and $Ca_{0.66}Mn_{1.6}Al_{0.4}O_4$ (in blue) compounds (recorded with a magnetic field from 0 to 50K Oe at 4K).

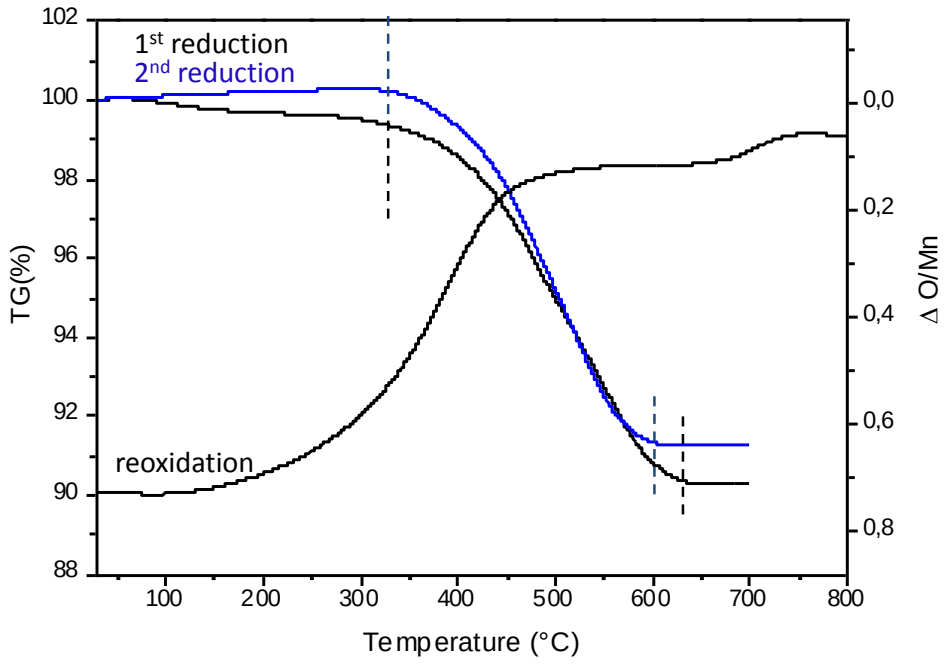

Figure 9: Thermogravimetric analysis (TGA) of $Ca_{0.66}Mn_{1.6}Al_{0.4}O_4$ oxide under Ar/H_2 5% flow and under air from room temperature to 700 °C. In blue, the second reduction under Ar/H_2 5% flow rate from room temperature to 700°C. The ΔO/Mn (exchanged oxygen per manganese) is also mentioned. The temperature range and the Δm/m (Table 5) are determined between the dash lines (black and blue).

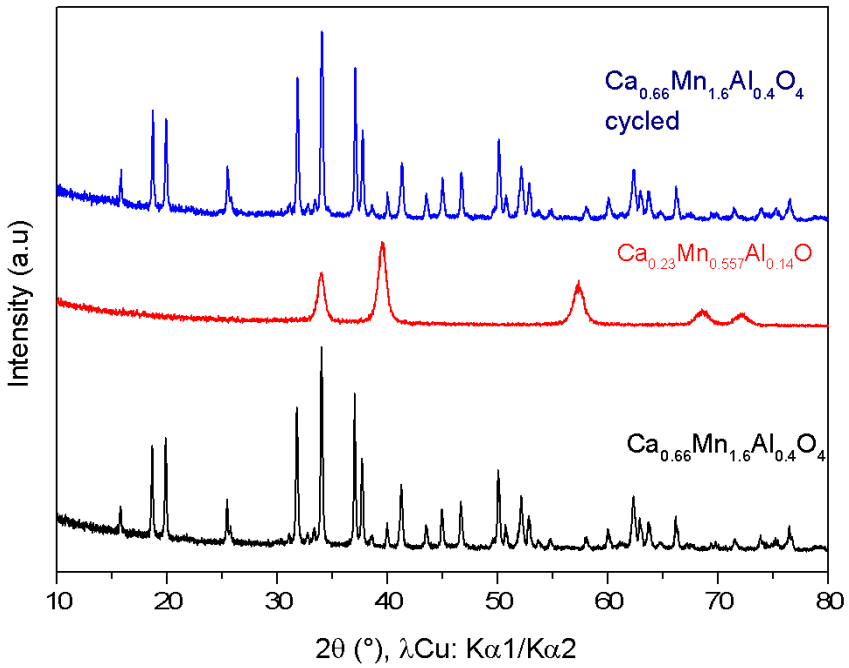

Figure 10: X-ray powder diffraction patterns of the $Ca_{0.66}Mn_{1.6}Al_{0.4}O_4$ oxide (orthorhombic unit cell, SG: *Pnma*) (in black), $Ca_{0.23}Mn_{0.5}Al_{0.14}$ O (Cubic unit cell, *Fm-3m*) obtained after TGA experiment (Figure 7) and finally the $Ca_{0.66}Mn_{1.6}Al_{0.4}O_4$ oxide (in blue) observed after re-oxidation showing the cyclability of this system.

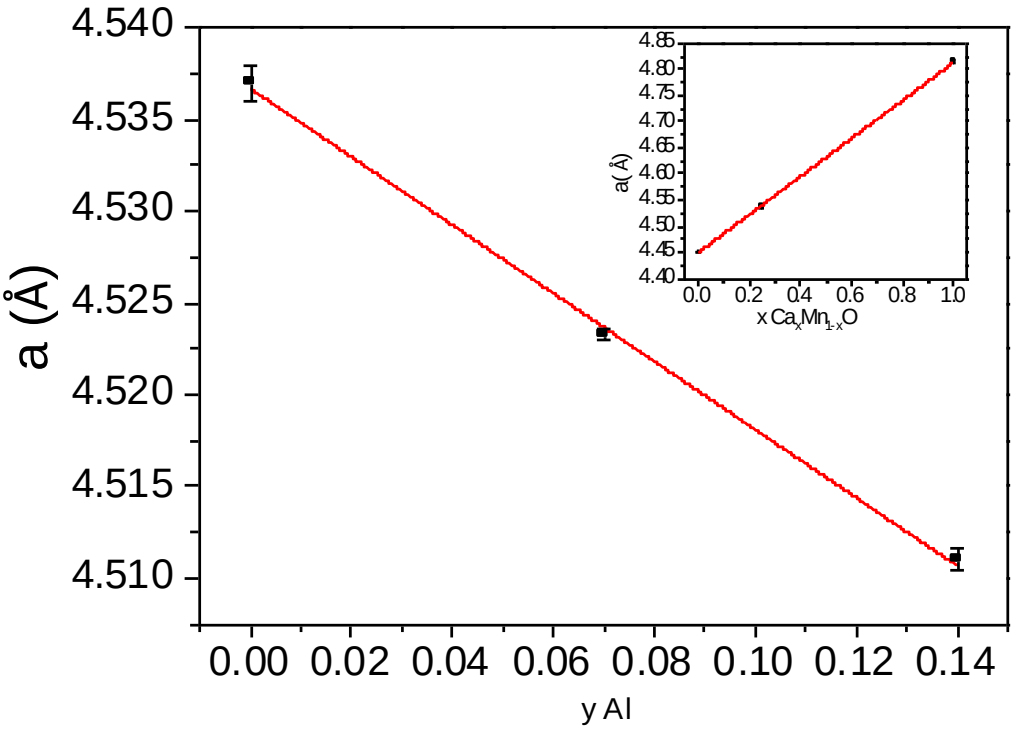

Figure 11: Variation of the unit cell parameter for $Ca_{0.25}Mn_{0.75}O$ (y=0), $Ca_{0.24}Mn_{0.65}Al_{0.07}O$ (y=0.07), $Ca_{0.23}Mn_{0.56}Al_{0.14}O$ (y=0.14) versus Al (y) content and $Ca_xMn_{1-x}O$ (x=0, 0.25, 1) compounds versus Ca (x) rate following a Vegard law.

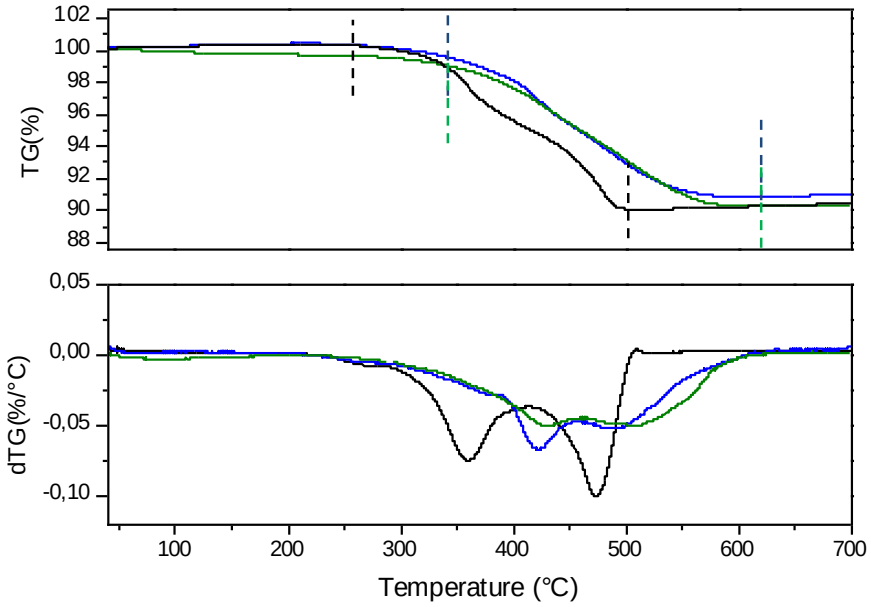

Figure 12: Thermogravimetric analysis (TGA) and the derivative curves (dTG) of $Ca_{0.66}Mn_2O_4$ (in black), $Ca_{0.66}Mn_{1.8}Al_{0.2}O_4$ (in blue) and $Ca_{0.66}Mn_{1.6}Al_{0.4}O_4$ (in green) oxides under Ar/H_2 5% flow. The temperature range and the $\Delta m/m$ (Table 6) are determined between the dash lines (black, blue and green) for each compound.

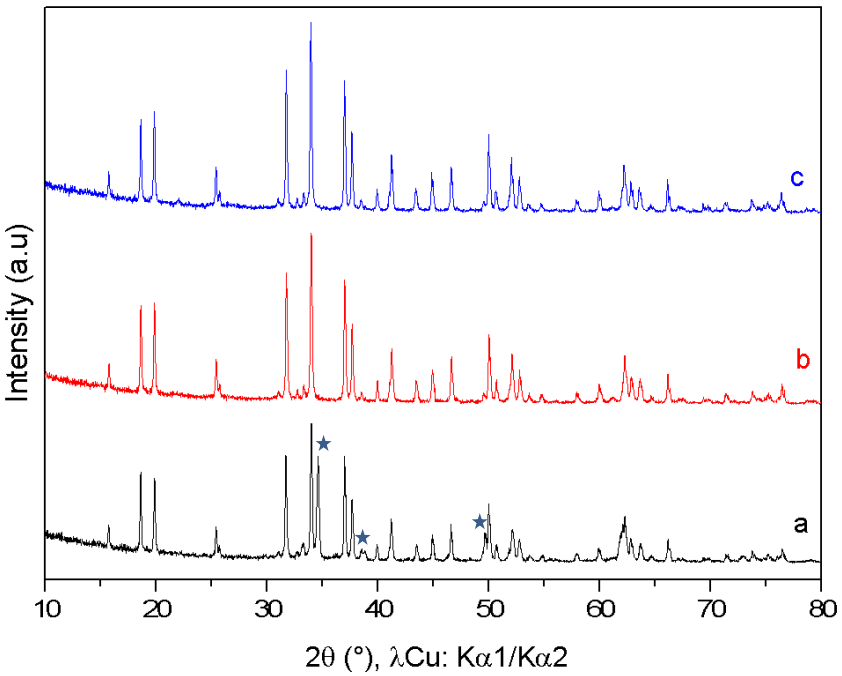

Figure 13: X-ray powder diffraction patterns of a) $Ca_{0.6}Mn_{1.8}Al_{0.2}O_4$. b) $Ca_{0.66}Mn_{1.8}Al_{0.2}O_4$ and c) $Ca_{0.7}Mn_{1.8}Al_{0.2}O_4$ compounds. For the composition $Ca_{0.6}Mn_{1.8}Al_{0.2}O_4$ the diffraction peaks of the impurity considered as Brownmillerite-type (SG: *Imma*) phase ($Ca_2(Mn,Al)_2O_5$) are marked by a star.

Table captions

Table 1: Atomic positions and unit cell parameters determined by Rietveld (Figures 4a and 4b) from powder X-Ray diffraction data of $Ca_{0.66}Mn_{2-x}Al_xO_4$ (x=0.2 and x=0.4) oxides. The reliability factors CRp. CRpw and RBragg are mentioned. Structural hypothesis: all Al atoms are located in Mn2 site (Mn^{4+}).

Atoms	Wyckoff positions	x (Al)	x	y	z	Biso [Å^2]	occupancy
Ca1	4c	0.2	0.2439(2)	¼	0.3324(1)	2..87(5)	0.66
		0.4	0.2439(4)	¼	0.3315(2)	4.49(9)	0.66
Mn1	4c	0.2	0.0692(1)	¼	0.11123(6	0.32(1)	1
		0.4	0.0701(2)	¼	0.1105(1))	0.28(1)	1
Mn2	4c	.2	0.0837(1)	¼	0.59452(7)	0.32(1)	0.8
		0.4	0.0841(2)	¼	0.0841(2)	0.28(1)	0.6
Al2	4c	0.2	0.0837(1)	¼	0.59452(7)	0.32(1)	0.2
		0.4	0.0841(2)	¼	0.5942(1)	0.28(1)	0.4
O1	4c	0.2	0.2935(3)	¼	0.6506(2)	0.39(2)	1
		0.4	0.2933(5)	¼	0.6497(4)	1.14(5)	1
O2	4c	0.2	0.3827(3)	¼	0.9781(2)	0.39(2)	1
		0.4	0.3814(4	¼	0.9761(4)	1.14(5)	1
O3	4c	0.2	0.4740(3)	¼	0.1977(2)	0..39(2)	1
		0.4	0.4747(5)	¼	0.1970(4)	1.14(5)	1
O4	4c	0.2	0.0712(4)	¼	0.9152(2)	0.39(2)	1
		0.4	0.0705(6)	¼	0.9153(3)	1.14(5)	1

Cell parameters (S.G: Pnma):

	a(Å)	b(Å)	c(Å)	V(Å^3
xAl : 0.2	8.9660(2)	2.82493(4)	11.2881(2)	285.908(8
xAl : 0.4	8.9532(3)	2.8238(1)	11.2802(4)	285.20(1)

Reliability Factors:

	CRp	CRwp	RBragg
xAl : 0.2	15.8%	13.1 %	8.79%
xAl : 0.4	16.9%	14.0%	7.00%

Table 2: Bond distances and valence determined from Table 1 (Rietveld refinement) of $Ca_{0.66}Mn_{2-x}Al_xO_4$ (x=0.2 and x=0.4) oxides. The average <Mn-O> and <Ca-O> bonds distances as well as the average of the difference between main distance and average distance are mentioned. Structural hypothesis: all Al atoms are located in Mn2 site (Mn^{4+}).

Distances (Å)		
x(Al)	**0.2**	**0.4**
Mn(1)-O1	**1.925(1) x 2**	**1.919(3)x 2**
Mn(1)-O3	**2.318(3)**	**2.333(4)**
Mn(1)-O4	**1.915(2)x 2**	**1.914(4)x 2**
	2.212(2)	**2.200(3)**
<Mn(1)-O>	**2.035**	**2.033**
|Mn(1)-O - <Mn(1)-O>|/6	**0.153**	**0.155**
Brown bond valence	**3.10**	**3.13**
M(2)-O1	**1.980(2)**	**1.975(5)**
M(2)-O2	**1.951(1)x 2**	**1.965(3)x 2**
	1.979(2)	**1.980(5)**
M(2)-O3	**1.903(2)x 2**	**1.901(3)x 2**
<M(2)-O>	**1.945**	**1.948**
|M(2)-O - <M(2)-O>|/6	**0.028**	**0.031**
Ca(1)-O1	**2.512(2)x 2**	**2.511(4) x 2**
Ca(1)-O2	**2.457(3) x 2**	**2.433(4) x 2**
Ca(1)-O3	**2.440(3)**	**2.432(6)**
	2.570(3)	**2.562(2)**
Ca(1)-O4	**2.362(3)x 2**	**2.376(5) x 2**
<Ca(1)-O>	**2.459**	**2.545**
|Ca(1)-O - <Ca(1)-O>|/8	**0.054**	**0.055**
Brown bond valence sum	**2.15**	**2.17**

Table 3: Theoretical result of magnetic parameters and summary of the Fitting Results using b) an ideal Curie Weiss law and c) a Curie Weiss with Temperature Independant Paramagnetic term (C.W*: Curie Weiss. TIP*:Temperature Independant Paramagnetism).

$Ca_{0.66}Mn_{2-x}Al_xO$	a) Expected values for an Isolated ions		b) Fitting with C.W* law					c) Fitting with C.W law with TIP*				
	C	μSO (μ_B/Mn)	C	μeff (μ_B/Mn)	Θ_P (K)	C	r^2	μeff (μ_B/Mn)	Θ_P (K)	TIP* (10^{-3}) Emu/mol.Mn	χ^2 (10^{-10})	r^2
x=0	2.6	4.58	2.89	4.81	-600	1.51±0.14	0.9982	3.51	-231±22	2.3±1.5.10^{-4}	3.73	0.9983
x=0.2	2.58	4.54	2.31	4.30	-300	2.07±0.09	0.9998	4.06	-157±10	1.3±1.1.10-4	0.51	0.9998
x=0.4	2.55	4.50	2.22	4.22	-200	1.64±0.04	0.9995	3.62	-52±4	2±6.10^{-5}	5.3	0.9997

Table 4: Main angles Mn^{3+}-O-Mn^{4+} (interchains) of a) $Ca_{0.66}Mn_2O_4$ and b) $Ca_{0.66}Mn_{1.8}Al_{0.2}O_4$ and $Ca_{0.66}Mn_{1.6}Al_{0.4}O_4$ determined from Rietveld refinements of powder X-Ray diffraction data (Figure S1. Table S1. Figures 4a-b and Tables 2a-b).

a) angles Mn-O-Mn (°)	**Mn^{3+}(1)-O1-Mn^{4+}(3)**	**Mn^{3+}(5)-O5-Mn^{4+}(3)**	**Mn^{3+}(1)-O6-Mn^{4+}(6)**	**Mn^{3+}(2)-O9-Mn^{4+}(6)**
$Ca_{0.66}Mn_2O_4$	132.4(9)	128.3(6)	133.4(7)	128.5(9)
b) angles Mn-O-Mn (°)	**$(Mn^{3+})_{site1}$-O1-$(Mn^{4+}/Al^{3+})_{site\ 2}$**		**$(Mn^{3+})_{site1}$-O1-$(Mn^{4+}/Al^{3+})_{site\ 2}$**	
$Ca_{0.66}Mn_{1.8}Al_{0.2}O_4$	122.3(1)		131.9(2)	
$Ca_{0.66}Mn_{1.6}Al_{0.4}O_4$	122.0(2)		131.9(2)	

Table 5: Thermogravimetric analysis (TGA. Figure 10) values of $Ca_{0.66}Mn_{1.6}Al_{0.4}O_4$ oxide reduced with Ar/H_2 5% flow (heating rate 5°C/min) then oxidized under air (heating rate 5°C/min) from room temperature to 700°C. The ΔO (exchanged oxygen atom per manganese) theoretical values have been estimated by considering the total reduction of $Mn^{3+/4+}$ into Mn^{2+}.

Sample: 1st reduction	**Δm/m**		**ΔO per Mn**		**Temperature range of reduction**
	Theo	**Exp**	**Theo**	**Exp**	
$Ca_{0.66}Mn_{1.6}Al_{0.4}O_4$	9.6%	9.5%	0.71	0.7	**325°C-640°C**
Sample Oxidation after the first reduction	**Δm/m**		**ΔO per Mn**		**Temperature range of oxidation**
	Theo	**Exp**	**Theo**	**Exp**	
$Ca_{0.23}Mn_{0.56}Al_{0.14}O$	9.6%	9.1%	0.71	0.67	**150°C-800°C**
Sample 2nd reduction	**Δm/m**		**ΔO per Mn**		**Temperature range of reduction**
	Theo	**Exp**	**Theo**	**Exp**	
$Ca_{0.66}Mn_{1.6}Al_{0.4}O_4$	9.6%	9.1%	0…71	0.67	**325°C-600°C**

Table 6: Thermogravimetric analysis (TGA Figure 12) values of $Ca_{0.66}Mn_2O_4$, $Ca_{0.66}Mn_{1.8}Al_{0.2}O_4$ and $Ca_{0.66}Mn_{1.6}Al_{0.4}O_4$ oxides reduced with Ar/H_2 5% flow (heating rate 2°C/min) from room temperature to 700°C. The ΔO (exchanged oxygen atom per manganese) theoretical values have been estimated by considering the total reduction of $Mn^{3+/4+}$ into Mn^{2+}.

Sample	**Δm/m**		**ΔO per Mn**		**Temperature range of reduction**
	Theo	**Exp**	**Theo**	**Exp**	
$CaMn_3O_6$	10.65%	10.55%	0.66	0.65	250°C-500°C
$Ca_{0.66}Mn_{1.8}Al_{0.2}O_4$	10.1%	98%	0.68	0.66	350°C-640°C
$Ca_{0.66}Mn_{1.6}Al_{0.4}O_4$	9.6%	9.2%	0.71	0.68	350°C-640°C